



Grid-side current harmonic suppression based on Butterworth filter and quasi-proportional resonance controller

FENG ZHAO¹, JIANING ZHANG¹  , XIAOQIANG CHEN^{1,2}, YING WANG^{1,2}

¹*School of Automation and Electrical Engineering, Lanzhou Jiaotong University
Lanzhou, China*

²*Key Laboratory of Opto-Technology and Intelligent Control Ministry of Education
Lanzhou, China*

e-mail: 2271741151@qq.com

(Received: 20.05.2022, revised: 13.07.2022)

Abstract: In order to meet the lightweight requirements of high-speed trains, the inductance-capacitance (LC) resonance circuits are cancelled in the traction drive system of some high-speed electric multiple units (EMUs) in China, which will lead to large low-order current harmonics on the grid side in the traction drive system of EMUs, seriously affecting the power quality. Therefore, the low-order harmonic current of the traction drive system of an EMU is studied in this paper. Firstly, the working principle of a four-quadrant pulse rectifier in a traction drive system is analyzed, and then the generation mechanism of low-order current harmonics on the grid side is studied deeply. Secondly, the voltage outer loop and current inner loop control of a four-quadrant pulse rectifier are optimized respectively. In the voltage outer loop control, a Butterworth filter is designed to suppress the beat frequency voltage of the DC side voltage, so as to indirectly suppress the low-order current harmonics. In the current inner loop, a quasi-proportional resonance (PR) controller with harmonic compensation is used to suppress low-order current harmonics, and a novel low-order current harmonics suppression strategy based on the Butterworth filter and quasi-PR controller is proposed. Finally, the results of the simulated validation of the proposed control strategy show that compared with the existing method of the notch filter + PR controller, the proposed optimal control strategy has a better effect on low-order current harmonic suppression, and improves the dynamic performance of the control system, further showing the correctness and effectiveness of the optimal control strategy.

Key words: Butterworth filter, current harmonic suppression, high-speed electric multiple units, quasi-PR controller, traction drive system



© 2022. The Author(s). This is an open-access article distributed under the terms of the Creative Commons Attribution-NonCommercial-NoDerivatives License (CC BY-NC-ND 4.0, <https://creativecommons.org/licenses/by-nc-nd/4.0/>), which permits use, distribution, and reproduction in any medium, provided that the Article is properly cited, the use is non-commercial, and no modifications or adaptations are made.

1. Introduction

When the EMU is in traction operation, the pantograph transmits 27.5 kV single-phase AC power from the catenary to the traction transformer, and the step-down output of the traction transformer is 1770 V single-phase AC power to the four-quadrant pulse rectifier. The pulse rectifier transforms the single-phase AC into DC, and transmits 3600 V DC to the traction inverter through the intermediate DC circuit. The traction inverter outputs a three-phase alternating current with adjustable voltage and frequency to drive the traction motor, thus enabling the EMU to operate. The traction drive system of a high-speed EMU is shown in Fig. 1.

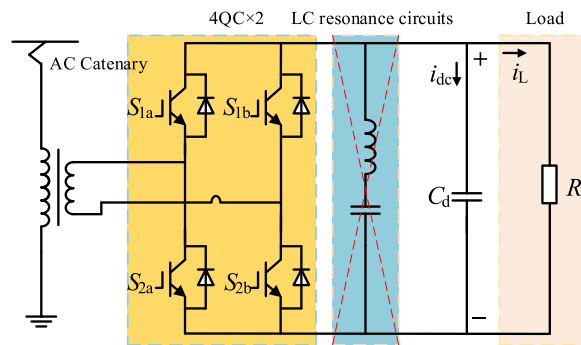


Fig. 1. Traction drive system of high-speed EMU

Due to the inherent internal structure characteristics, the output voltage of the DC side of the four-quadrant pulse rectifier has a 100 Hz AC voltage component, namely the beat frequency voltage [1, 2]. At present, the existing trains incorporate an LC resonant circuit in the middle DC link to absorb the beat frequency voltage of DC voltage. The resonant frequency of an LC resonance circuit is near 100 Hz if the value of inductance and capacitance is reasonably designed. Then the beat frequency component of DC voltage can be absorbed by series resonance to weaken the influence of beat frequency voltage on the current at the grid side. This method can reduce the beat frequency component of the DC voltage from the root. However, the volume and mass of the LC resonant circuit are large, which increases the weight and cost of the EMU, makes it not conducive to the maintenance of the hardware circuit, causes poor reliability, and goes against the requirements of lightweight trains. Therefore, LC resonance circuits are not installed in some China's high-speed EMUs. However, the beat frequency voltage cannot be filtered after the use of the LC resonant circuit is discontinued. For the rectifier, due to the introduction of beat frequency voltage in the control system, the grid-side current causes the 3rd harmonic [3–5], and the 3rd harmonic introduces the 5th harmonic. By analogy, 3rd, 5th, 7th and other low order harmonics will exist in the grid side current, which will reduce the current quality and seriously affect the safety of train running.

In the Beijing bullet train section in 2012, due to the simultaneous hosting of multiple trains, the traction network contained a large amount of low-order harmonic current, and the serious harmonic pollution of the power grid resulted in the start failure of the EMU traction converters placed in the same power supply range. It can be seen that the low-order harmonic current on the

grid side seriously affects the operation of traction drive systems and is not conducive to the safe and reliable operation of railway systems. Therefore, domestic and foreign scholars have carried out a lot of research on this. For example, in references [6] and [7], a C-type filter is proposed to solve the problem of harmonic resonance and low frequency characteristic harmonics by establishing a mathematical model and optimizing topological structure respectively, which can effectively solve the problem of harmonic without introducing any power loss. In order to reduce the influence of the beat frequency voltage on the control system and suppress the low-order current harmonics, the method of adding a double-traction network frequency 100 Hz notch filter is adopted in the voltage signal feedback link at the DC side in references [8] and [9]. References [10], [11] and [12] use a repetitive controller in the current inner loop, which reduces the current harmonics on the grid side, but also lowers the dynamic performance of the system. Model predictive control [13] can solve the problem of slow dynamic response, is suitable for nonlinear constrained control, and has the advantage of a simple control objective [14–16], so it is often used in pulse-width modulation (PWM) rectifiers [17, 18]. However, model predictive control cannot effectively suppress low order current harmonics because the control quantity is a fundamental wave component. Therefore, the rectifier control strategy of the notch filter + PR controller is adopted in reference [19], which reduces the low-order current harmonics on the basis of improving the dynamic performance of the system. However, notch filters can only filter the beat component of specific frequency in the DC voltage, so its suppression effect still needs to be improved.

By summarizing the methods used in the above literature, it can be seen that for the four-quadrant pulse rectifier controlled by a voltage and current double-closed loop, there are roughly two types of suppression strategies: one is to add compensation to the inner current loop such as introducing a repetitive controller, proportional resonance control and other methods [20, 21], but such methods will affect the dynamic performance of the system. Another type of method is to filter out the beat frequency voltage before DC side voltage appears in the control system [22, 23], such as adding a notch filter, low-pass filter, or dynamic compensation for the DC side voltage, etc. These methods can effectively solve the problem of slow dynamic response but compared to the LC resonance circuit, the low-order current harmonic suppression effect is poorer.

In order to solve the problem that the effectiveness of harmonic suppression and the rapidity of the dynamic performance of the system cannot be considered simultaneously by the above two types of suppression strategies, a low-order current harmonic suppression strategy based on the Butterworth Filter and quasi-PR controller with harmonic compensation is proposed in this paper. This method not only effectively suppresses the low-order current harmonics, but also improves the dynamic response of the system. It is beneficial to improve the power quality of the grid side, and is of great significance to ensure the safe and stable operation of the EMU.

In this paper, the internal traction drive system of the EMU is taken as the research object, and the low-order current harmonics of the transformer's secondary side, caused by the beat frequency voltage of a four-quadrant pulse rectifier DC side, are suppressed. The paper is organized as follows: the working principle of a four-quadrant pulse rectifier is introduced in Section 2. The generation mechanism of low-order current harmonics in the grid side is analyzed in Section 3. The suppression method of low-order current harmonics is proposed in Section 4. Simulation results to prove the validity and feasibility of the proposed method are presented in Section 5. The conclusions of this paper are described in Section 6.

2. Working principle of four-quadrant pulse rectifier

The four-quadrant pulse rectifier is mainly composed of fully controlled devices and reverse parallel diodes [24], and its main circuit is shown in Fig. 2(a). R and L are the equivalent resistance and inductance of the secondary-side of the locomotive transformer. S_{1a} , S_{2a} , S_{1b} , S_{2b} represent the IGBT module in reverse parallel with the diode; C_d and R_L represent the supporting capacitance and load on the output-side of the four-quadrant pulse rectifier. u_s and i_s are the voltage and current of the secondary side of the locomotive transformer at the rectifier's grid side. u_{ab} is the input voltage of the AC side of the rectifier. U_{dc} is the output voltage of the DC side of the rectifier. i_L is the load current.

To facilitate analysis, the ideal switching function S_i ($i = a, b$) is defined as Eq. (1):

$$S_i = \begin{cases} 1, & S_{1i} \text{ on, } S_{2i} \text{ off} \\ 0, & S_{1i} \text{ off, } S_{2i} \text{ on} \end{cases} \quad (i = a, b). \quad (1)$$

According to the ideal switching function S_i in Eq. (1), the main circuit in Fig. 2(a) is equivalent to the obtained equivalent circuit, as shown in Fig. 2(b). Because S_{1i} and S_{2i} cannot be turned on at the same time in the four-quadrant pulse rectifier, the value of the input voltage u_{ab} can be U_{dc} , 0 and $-U_{dc}$, and the switch combination $S_a S_b$ can be 00, 01, 10 and 11, altogether 4 kinds of logistics. The input terminal voltage u_{ab} can be obtained as shown in Eq. (2):

$$u_{ab} = (S_a - S_b) U_{dc}. \quad (2)$$

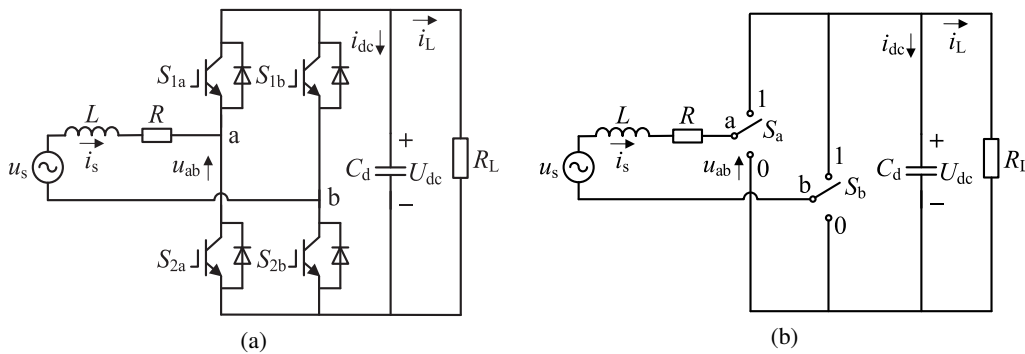


Fig. 2. Topology of four-quadrant pulse rectifier: the main circuit diagram (a); switch equivalent circuit diagram (b)

Kirchhoff's law is adopted to analyze the circuit in Fig. 2(b), and the mathematical model of the main circuit of the rectifier can be obtained as shown in Eq. (3):

$$\begin{cases} L \frac{di_s}{dt} + i_s R = u_s - (S_a - S_b) U_{dc} \\ C_d \frac{dU_{dc}}{dt} = (S_a - S_b) i_s - \frac{U_{dc}}{R_L} \end{cases}. \quad (3)$$

Therefore, the state equation of the mathematical model of the four-quadrant pulse rectifier is as shown in Eq. (4):

$$\begin{bmatrix} \dot{i}_s \\ \dot{U}_{dc} \end{bmatrix} \begin{bmatrix} -R/L & -(S_a - S_b)/L \\ (S_a - S_b)/C_d & -1/C_d R_L \end{bmatrix} \begin{bmatrix} i_s \\ U_{dc} \end{bmatrix} + \begin{bmatrix} 1/L \\ 0 \end{bmatrix} u_s. \quad (4)$$

3. Generation mechanism of low-order current harmonics in grid side

The current harmonics of the grid side are the main source of harmonic pollution in the traction power supply network. If only the fundamental wave content and the integral multiple harmonic component of the fundamental wave are considered, the voltage u_s and current i_s of the grid side can be expressed as shown in Eqs. (5) and (6):

$$u_s = \sqrt{2}U_s \cos \omega t + \sum_{k=2}^n \sqrt{2}U_{sk} \cos k\omega t, \quad (5)$$

$$i_s = \sqrt{2}I_s \cos(\omega t - \varphi) + \sum_{k=2}^n \sqrt{2}I_{sk} \cos(k\omega t - \varphi_k), \quad (6)$$

where: U_s and I_s are the effective values of fundamental wave voltage and current at the grid side; U_{sk} and I_{sk} are the effective values of harmonic voltage and current at the k -th harmonic; φ is the included angle between fundamental wave voltage and current; φ_k is the included angle between voltage and current of the k -th harmonic; ω represents the angular frequency of the traction network voltage.

Since the amplitude of voltage and current harmonics is very small, if the product of the harmonic voltage and current $U_{sk} I_{sk}$ is ignored, the input power of the rectifier can be obtained as shown in Eq. (7):

$$\begin{aligned} P_{in} \approx & U_s I_s \cos \varphi + U_s I_s \cos(2\omega t - \varphi) + 2I_s \sum_{k=2}^n U_{sk} \cos k\omega t \cos(\omega t - \varphi) \\ & + 2U_s \sum_{k=2}^n I_{sk} \cos(k\omega t - \varphi_k) \cos \omega t. \end{aligned} \quad (7)$$

In addition, according to the circuit structure of the rectifier in Fig. 2(a), its output power P_{out} is as shown in Eq. (8):

$$P_{out} \approx \bar{U}_{dc} \bar{I}_L + C_d \bar{U}_{dc} \frac{d\bar{u}_{dc}}{dt}. \quad (8)$$

where: \bar{I}_L is the average value of the load current; \bar{U}_{dc} is the average value of the rectifier output voltage U_{dc} ; \bar{u}_{dc} is the fluctuation value of U_{dc} .

Assuming an ideal switching device is used, the input and output power are conserved. Eq. (9) can be obtained from the equal dynamic components of input and output power:

$$C_d \bar{U}_{dc} \frac{d\tilde{u}_{dc}}{dt} = U_s I_s \cos(2\omega t - \varphi) + 2I_s \sum_{k=2}^n U_{sk} \cos k\omega t \cos(\omega t - \varphi) + 2U_s \sum_{k=2}^n I_{sk} \cos(k\omega t - \varphi_k) \cos \omega t. \quad (9)$$

Therefore, the beat frequency voltage \tilde{u}_{dc} of the DC side is as shown in Eq. (10):

$$\begin{aligned} \tilde{u}_{dc} = & \frac{U_s I_s}{2\omega C_d \bar{U}_{dc}} \sin(2\omega t - \varphi) \\ & + \frac{I_s}{\omega C_d \bar{U}_{dc}} \left\{ \sum_{k=2}^n \frac{U_{sk}}{k+1} \sin[(k+1)\omega t - \varphi] + \sum_{k=2}^n \frac{U_{sk}}{k-1} \sin[(k-1)\omega t + \varphi] \right\} \\ & + \frac{U_s}{\omega C_d \bar{U}_{dc}} \left\{ \sum_{k=2}^n \frac{I_{sk}}{k+1} \sin[(k+1)\omega t - \varphi_k] + \sum_{k=2}^n \frac{I_{sk}}{k-1} \sin[(k-1)\omega t + \varphi_k] \right\}. \quad (10) \end{aligned}$$

According to Eq. (10), there are two kinds of harmonics in the voltage ripple on the DC side. One is the harmonic with twice the grid voltage frequency, that is, 100 Hz; The other is the harmonic component produced by the interaction of voltage harmonics and current harmonics on the grid side. Therefore, the existence of voltage ripples will introduce current harmonics on the grid side.

In order to simplify the analysis, the PI controller in the voltage outer loop control of the rectifier is simplified as the P controller, and the given current value i_s^* on the grid side can be calculated as shown in Eq. (11):

$$\begin{aligned} i_s^* &= I_{sm}^* \cos \omega t = K_{VP} \left(U_{dc}^* - \bar{U}_{dc} - \tilde{u}_{dc} \right) \cos \omega t \\ &= K_{VP} \left(U_{dc}^* - \bar{U}_{dc} \right) \cos \omega t - K_{VP} \tilde{u}_{dc} \cos \omega t, \quad (11) \end{aligned}$$

where: I_{sm}^* is the amplitude of the given current value; K_{VP} is the proportional coefficient of the P controller; U_{dc}^* is the given value of the voltage on the DC side.

By substituting in Eq. (10) into Eq. (11) and arranging, Eq. (12) can be obtained as:

$$\begin{aligned} i_s^* &= K_{VP} \left(U_{dc}^* - \bar{U}_{dc} \right) \cos \omega t - \frac{K_{VP} U_s I_s}{4\omega C_d \bar{U}_{dc}} \sin(\omega t - \varphi) - \frac{K_{VP} U_s I_s}{4\omega C_d \bar{U}_{dc}} \sin(3\omega t - \varphi) \\ &- \frac{K_{VP} I_s}{2\omega C_d \bar{U}_{dc}} \left\{ \sum_{k=2}^n \frac{U_{sk}}{k+1} \sin[(k+2)\omega t - \varphi] + \sum_{k=2}^n \frac{U_{sk}}{k+1} \sin(k\omega t - \varphi) \right. \\ &\quad \left. + \sum_{k=2}^n \frac{U_{sk}}{k-1} \sin(k\omega t + \varphi) + \sum_{k=2}^n \frac{U_{sk}}{k-1} \sin[(k-2)\omega t + \varphi] \right\} \\ &- \frac{K_{VP} U_s}{2\omega C_d \bar{U}_{dc}} \left\{ \sum_{k=2}^n \frac{I_{sk}}{k+1} \sin[(k+2)\omega t - \varphi_k] + \sum_{k=2}^n \frac{I_{sk}}{k+1} \sin(k\omega t - \varphi_k) \right. \\ &\quad \left. + \sum_{k=2}^n \frac{I_{sk}}{k-1} \sin(k\omega t + \varphi_k) + \sum_{k=2}^n \frac{I_{sk}}{k-1} \sin[(k-2)\omega t + \varphi_k] \right\}. \quad (12) \end{aligned}$$

Due to the error-free control of the inner current loop, the harmonic distribution of the actual current at the grid side is the same as that of the given value in the steady state. If the harmonic of the voltage and current at the grid side is not considered, namely $U_{sk} = I_{sk} = 0$ ($k = 2, 3, 4, \dots, n$), then, Eq. (12) can be simplified as shown in Eq. (13):

$$i_s^* = K_{vP} \left(U_{dc}^* - \bar{U}_{dc} \right) \cos \omega t - \frac{K_{vP} I_{Load}}{4\omega C_d \cos \varphi} \sin(\omega t - \varphi) - \frac{K_{vP} I_L}{4\omega C_d \cos \varphi} \sin(3\omega t - \varphi). \quad (13)$$

According to Eq. (13), when the voltage and current input from the AC side of the rectifier itself does not have harmonics, the grid side current contains only the 3rd harmonic.

If the traction network current itself contains the 3rd harmonic, that is $I_{s3} \neq 0$, the expression of the current at the grid side can be obtained from Eq. (12), as shown in Eq. (14):

$$i_s^* = I_{sm}^* \cos \omega t = K_{vP} \left(U_{dc}^* - \bar{U}_{dc} \right) \cos \omega t - \frac{K_{vP} U_s I_s}{4\omega C_d \bar{U}_{dc}} \sin(\omega t - \varphi) - \frac{K_{vP} U_s I_s}{4\omega C_d \bar{U}_{dc}} \sin(3\omega t - \varphi) - \frac{K_{vP} U_s I_{s3}}{2\omega C_d \bar{U}_{dc}} \left[\frac{1}{4} \sin(5\omega t - \varphi_3) + \frac{1}{4} \sin(3\omega t - \varphi_3) + \frac{1}{2} \sin(3\omega t + \varphi_3) + \frac{1}{2} \sin(\omega t + \varphi_3) \right]. \quad (14)$$

According to Eq. (14), the 3rd harmonic of the grid side current will introduce the 5th harmonic of the current. Similarly, by substituting the 5th harmonic into Eq. (12), it can be calculated that the grid side current has 7 harmonics, and the influence of beat frequency voltage on harmonic current of the grid side is shown in Fig. 3. Therefore, if the grid-side voltage background harmonics are not considered, the grid-side current of the four-quadrant pulse rectifier will contain odd current harmonics of 3rd, 5th, 7th, and so on [25].

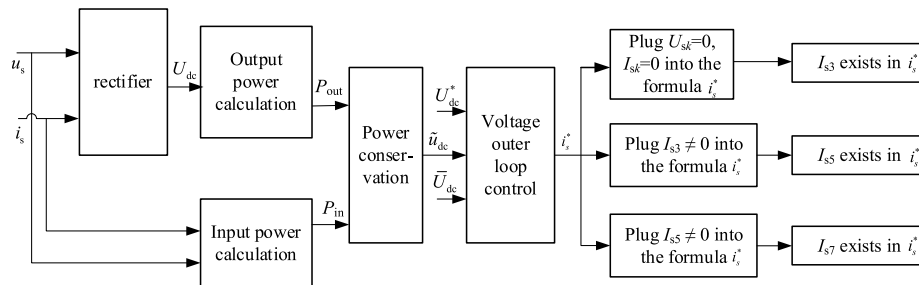


Fig. 3. The influence of beat frequency voltage on harmonic current of grid side

4. Suppression of low-order current harmonics in grid side

Because the four-quadrant pulse rectifier can be connected with the inverter and traction motor, it is often used in an AC drive electric locomotive to adapt to the speed regulation system which often needs traction and regenerative braking. Controlling the rectifier can keep the output DC voltage constant, and the power factor of the grid side tends to 1, which is beneficial to improve the economic benefit of the traction electric network. The four-quadrant pulse rectifier in the traction drive system adopts the transient direct current control method, and its core is

voltage and current double-closed loop control. Therefore, in this section, the control methods of the four-quadrant pulse rectifier are optimized from the aspects of the voltage outer loop and the current inner loop, respectively, to effectively suppress the low-order current harmonics.

4.1. Optimization control of voltage outer loop

1. Traditional voltage outer loop control

The function of voltage outer loop control is to make the four-quadrant pulse rectifier output a constant DC voltage, so that it is stable around a given value. Considering the small inertia link caused by sampling delay, the voltage outer loop controller is shown in Fig. 4.

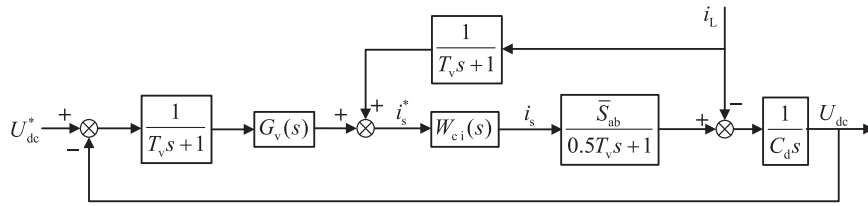


Fig. 4. Structure diagram of voltage outer loop controller

where: U_{dc}^* is the reference value of the DC side voltage; T_v represents the signal sampling period; $G_v(s)$ is the transfer function of the voltage outer loop controller. \bar{S}_{ab} represents the average of difference between switching functions S_a and S_b in the same period. If $G_v(s)$ is the transfer function of the PI controller commonly used in practical engineering, it is defined as shown in Eq. (15):

$$G_v(s) = \frac{K_{vP}s + K_{vI}}{s} = \frac{K_{vP}(\tau_v s + 1)}{\tau_v s}, \quad (15)$$

where K_{vP} and K_{vI} are the proportional and integral coefficients of the PI controller, respectively,

$$\tau_v = \frac{K_{vI}}{K_{vP}}.$$

In order to simplify the control structure in Fig. 4, the voltage sampling small inertia time constant T_v is combined with the current inner-loop equivalent time constant T_i , and the order is reduced, namely: $T_{ev} = T_v 3T_i$. Fig. 5 is the simplified structure.

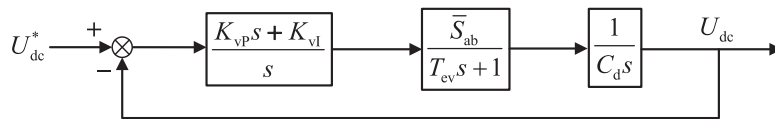


Fig. 5. Simplified voltage outer loop controller structure diagram

According to Fig. 5, the open loop transfer function $W_{ov}(s)$ of the voltage outer loop is shown in Eq. (16):

$$W_{ov}(s) = \frac{K_{vP}s + K_{vI}}{C_d s^2 (T_{ev}s + 1)} = \frac{K_{vP}(\tau_v s + 1)}{C_d \tau_v s^2 (T_{ev}s + 1)}. \quad (16)$$

Then, the closed-loop transfer function of the voltage outer loop is shown in Eq. (17):

$$W_{cv}(s) = \frac{W_{ov}(s)}{1 + W_{ov}(s)} = \frac{K_{vP}(\tau_v s + 1)}{C_d \tau_v T_{ev} s^3 + C_d \tau_v s^2 + K_{vP} \tau_v s + K_{vP}}. \quad (17)$$

2. Design of the Butterworth filter

The Butterworth filter has the characteristic that the frequency response curve in the passband is flat to the maximum without fluctuation, and decreases to zero in the stopband. The amplitude-frequency and phase-frequency characteristic curves of the filter decrease monotonically with the increase of frequency, and because the frequency response of the filter is relatively flat before the cutoff frequency, it has the advantage of ensuring that the original value of the signal will not be attenuated by filtering.

The amplitude-frequency response of the Butterworth filter shall satisfy Eq. (18):

$$|H(j\omega)|^2 = \frac{1}{1 + \left(\frac{\omega}{\omega_c}\right)^{2n}}, \quad (18)$$

where n is the order of the filter and ω_c is the cut-off frequency, that is, the frequency at which the amplitude drops to -3dB .

The constraint condition of the passband attenuation R_p and passband cut-off frequency ω_p of the Butterworth filter is shown in Eq. (19):

$$R_p = 20 \lg(1) - 20 \lg \left[\sqrt{\frac{1}{1 + \left(\frac{\omega_p}{\omega_c}\right)^{2n}}} \right]. \quad (19)$$

The constraint condition of the stopband attenuation A_s and stopband cut-off frequency ω_s is shown in Eq. (20):

$$A_s = 20 \lg(1) - 20 \lg \left[\sqrt{\frac{1}{1 + \left(\frac{\omega_s}{\omega_c}\right)^{2n}}} \right]. \quad (20)$$

Simultaneous Eqs. (19) and (20) can solve the order n of the Butterworth filter, as shown in Eq. (21):

$$n = \frac{\lg \left(\frac{10^{A_s/10} - 1}{10^{R_p/10} - 1} \right)}{2 \lg \left(\frac{\omega_s}{\omega_p} \right)}. \quad (21)$$

By rounding n up to n^* , and substituting n^* into Eq. (20), the cutoff frequency ω_c can be obtained, as shown in Eq. (22):

$$\omega_c = \left(10^{A_s/10} - 1 \right)^{-\frac{1}{2n^*}} \omega_s. \quad (22)$$

The unified form of the transfer function of the Butterworth filter is shown in Eq. (23):

$$H(s) = \frac{\omega_c^{n^*}}{a_0\omega_c^{n^*} + a_1\omega_c^{n^*-1}s + \dots + a_{n^*-1}\omega_c^1s^{n^*-1} + s^{n^*}} \quad (23)$$

Because the beat frequency voltage of 2, 4, 6 times of grid frequency mainly exists in the DC-side voltage of the four-quadrant pulse rectifier, and in practical engineering, the voltage near these three frequencies will also have small fluctuation, so the constraint conditions are set as: the passband cut-off frequency $\omega_p = 20\pi$ (rad/s), passband maximum attenuation $R_p = 1$ dB, stopband cut-off frequency $\omega_s = 160\pi$ (rad/s) and stopband minimum attenuation $A_s = 30$ dB. In this way, the beat voltage of grid frequency above 80 Hz in the actual DC voltage can be filtered before entering a PI controller, so as to indirectly suppress the low-order current harmonics on the grid side.

According to the constraints of ω_p , ω_s , R_p , A_s and Eqs. (21) and (22), the order of the Butterworth filter $n = 1.9856$, $\omega_c = 89.4084$ can be calculated, and $n^* = 2$.

The normalized polynomial coefficients of orders 1–4 of the Butterworth filter are shown in Table 1. By substituting the calculated $\omega_c = 89.4084$ and $n^* = 2$ into Eq. (23), and combining the coefficients corresponding to the order $n^* = 2$ in Table 1, the transfer function of the Butterworth filter designed in this paper can be obtained as shown in Eq. (24). The corresponding Bode diagram is shown in Fig. 6.

$$H(s) = \frac{7993.9}{s^2 + 126.4s + 7993.9} \quad (24)$$

Table 1. Normalized polynomial coefficient of Butterworth filter

n^*	a_0	a_1	a_2	a_3	a_4
1	1	1			
2	1	1.4142136	1		
3	1	2	2	1	
4	1	2.6131259	3.4142136	2.6131259	1

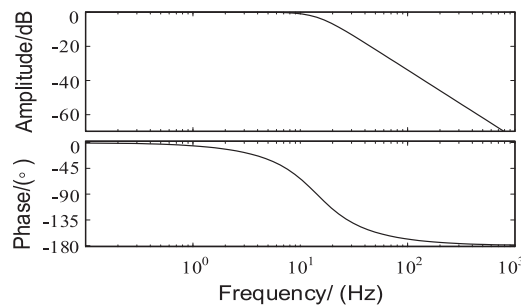


Fig. 6. The Bode diagram of Butterworth filter

After applying bilinear transformation to Eq. (24), the form of a digital Butterworth filter can be obtained as shown in Eq. (25):

$$H(z) = \frac{7993.9 (z^{-1})^2 + 15987.8z^{-1} + 7993.9}{7868.5 (z^{-1})^2 + 15985.8z^{-1} + 8121.3}. \quad (25)$$

4.2. Optimization control of current inner loop

1. Traditional current inner-loop control

The function of the current inner-loop control is to make the grid-side current track its given value, so that the grid-side power factor of the four-quadrant pulse rectifier approaches 1. Fig. 7 shows the structure of current inner loop control with sampling delay and small inertia characteristics included.

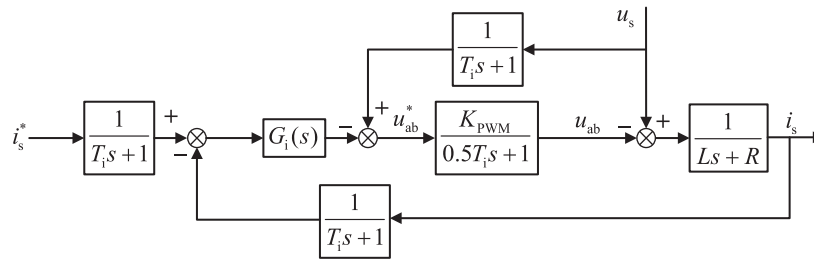


Fig. 7. Current inner loop control structure diagram

where: i_s^* is the given value of the grid-side current; T_i is the current sampling period; $G_i(s)$ is the transfer function of the current inner loop controller; u_{ab}^* is the control signal instruction value, and K_{PWM} represents the equivalent gain of the bridge PWM. The time constant of the small inertia link caused by the PWM is $T_i/2$; moreover, the feedforward voltage signal u_s also has sampling delay. Therefore, the current inner loop control of the voltage u_s feedforward can be simplified into the equivalent circuit shown in Fig. 8.

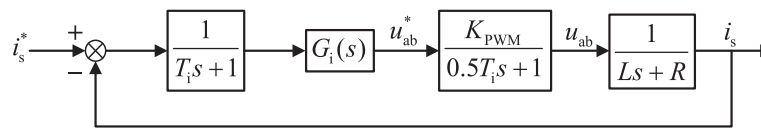


Fig. 8. Simplified current inner loop control structure diagram

According to Fig. 8, the open loop transfer function $W_{oi}(s)$ of the current inner loop is shown in Eq. (26):

$$W_{oi}(s) = \frac{K_{PWM} G_i(s)}{(T_i s + 1)(0.5 T_i s + 1)(Ls + R)}. \quad (26)$$

When designing the controller, combining the first-order inertia link of the PWM circuit and sampling circuit of the rectifier, and reducing its order, Eq. (26), can be simplified as shown

in Eq. (27):

$$W_{oi}(s) = \frac{K_{PWM}G_i(s)}{(0.5T_i^2s^2 + 1.5T_i s + 1)(Ls + R)} \approx \frac{K_{PWM}G_i(s)}{(1.5T_i s + 1)(Ls + R)}. \quad (27)$$

2. Optimized current inner-loop control

Because the current inner-loop input is AC, and the PI controller or P controller act on the rectifier current inner-loop control, only the DC can be effectively controlled, the AC error-free control is difficult to achieve and it does not meet the high precision control requirements. Therefore, in this paper, the PR controller is applied to the current inner-loop control to achieve error-free AC control.

If the angular frequency of the tracked signal is ω_0 , the transfer function of the ideal PR controller in the s -domain is as shown in Eq. (28), and its characteristic curves of amplitude-frequency and phase-frequency are shown in Fig. 9(a).

$$H_{PR}(s) = K_P + \frac{2K_R s}{s^2 + \omega_0^2}, \quad (28)$$

where K_P and K_R are the proportionality and resonance coefficients of the PR controller.

However, in addition to the 50 Hz fundamental current, the grid side also contains low-order current harmonics. Therefore, the PR controller needs to be improved to eliminate the 3rd, 5th and 7th current harmonics. Its transfer function in the s -domain is shown in Eq. (29). The amplitude-frequency and phase-frequency characteristic curves of the improved PR controller are shown in Fig. 9(b).

$$H_{PR}(s) = K_P + \frac{2K_R s}{s^2 + \omega_0^2} + \sum_{h=3,5,7} \frac{K_{Rh} s}{s^2 + (h\omega_0)^2}, \quad (29)$$

where K_{Rh} is the resonance coefficient of the h -th harmonic PR controller and h is the order of harmonics.

Because the ideal PR controller has the function of gaining a single frequency and attenuating other frequency signals, its system has a narrow bandwidth, so that the system is often disturbed and its stability is reduced. Therefore, a quasi-PR controller is needed to solve this problem. Its transfer function is shown in Eq. (30), and the corresponding amplitude-frequency and phase-frequency characteristic curves are shown in Fig. 9(c). Compared with Fig. 9(b), the bandwidth is significantly increased and the anti-interference capability of the system is improved.

$$H_{PR}(s) = K_P + \frac{2\omega_c K_R s}{s^2 + 2\omega_c s + \omega_0^2} + \sum_{h=3,5,7} \frac{2\omega_c K_{Rh} s}{s^2 + 2\omega_c s + (h\omega_0)^2}, \quad (30)$$

where ω_c is the cut-off frequency of the controller.

After comparing and analyzing the characteristics of PI and PR controllers, the quasi-PR controller with 3rd, 5th and 7th harmonics compensation is used in the current inner loop to suppress the low-order current harmonics. The optimized current inner-loop control block diagram is shown in Fig. 10.

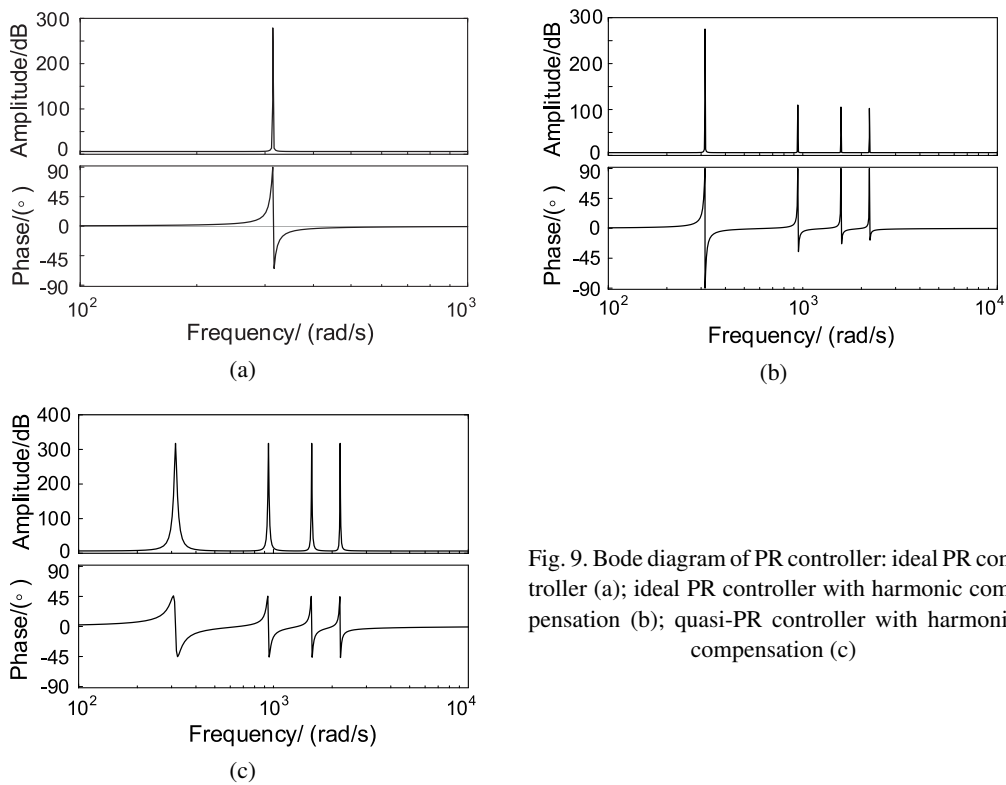


Fig. 9. Bode diagram of PR controller: ideal PR controller (a); ideal PR controller with harmonic compensation (b); quasi-PR controller with harmonic compensation (c)

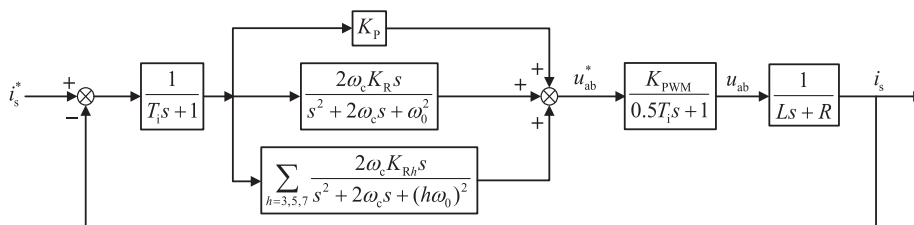


Fig. 10. Optimized current inner loop control diagram

4.3. Overall optimal control of four-quadrant pulse rectifier

Combined with the above optimization control methods of the voltage outer loop and current inner loop, a four-quadrant pulse rectifier control method based on the Butterworth filter and quasi-PR controller with harmonic compensation is proposed to suppress low-order current harmonics. Figure 11 is the concrete design block diagram. A Butterworth filter is added in the voltage outer loop control, so that the beat frequency voltage with a frequency greater than 80 Hz in the DC voltage is filtered out before entering the PI controller to indirectly suppress the low-order current harmonics. The current inner loop adopts the quasi-PR controller with 3rd, 5th and 7th harmonic

compensation, so that the actual current value can accurately track its given value and meet the no steady-state error tracking. The anti-interference ability of the current inner loop is enhanced, so as to effectively reduce the low-order harmonic current of the grid side.

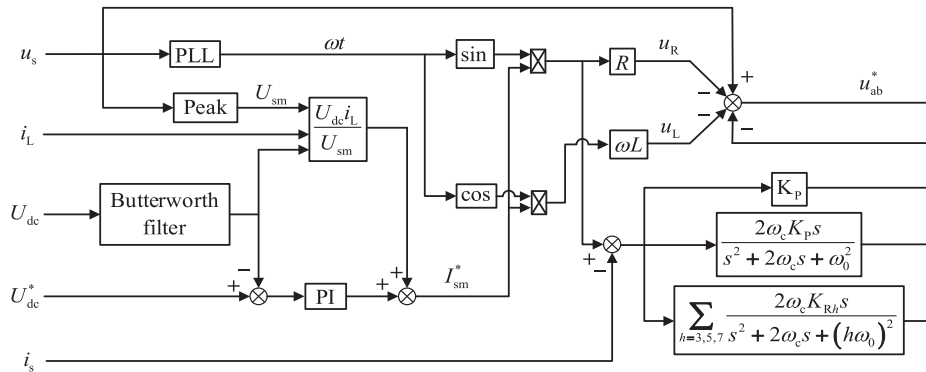


Fig. 11. Optimal control block diagram of four-quadrant pulse rectifier

5. Simulation results and analysis

The simulation model of an EMU four-quadrant pulse rectifier is built on Matlab/Simulink platform. Based on the theory of phase-shifting carrier technology, two four-quadrant pulse rectifiers are simulated in parallel. The simulation parameters are shown in Table 2.

Table 2. Simulation parameters of rectifier

Parameter name	Symbol	Value	Unit
Effective value of the AC side voltage	U_s	1770	V
AC side inductance	L	5.5	mH
Reference value of DC side voltage	U_{dc}^*	3 600	V
DC side support capacitor	C_d	9.01	mF
Voltage loop PI controller proportional coefficient	K_{vP}	0.8	/
Voltage loop PI controller integral coefficient	K_{vI}	15	/
Proportionality coefficient of quasi-PR controller	K_P	2	/
Resonance coefficient of quasi-PR controller	K_R/K_{Rh}	110	/

5.1. Four-quadrant pulse rectifier control performance verification

Figure 12(a) shows the voltage and current waveform of transforming from traction condition to braking condition at $t = 0.6$ s after using the Butterworth filter and quasi-PR controller with harmonic compensation. When the time ranges from 0.1 s to 0.6 s, the voltage and current at the

AC side of the rectifier are in the same phase at the traction condition. Figure 12(b) shows the amplification of voltage and current waveforms near $t = 0.6$ s. At $t = 0.6$ s, a reverse voltage is added to the output DC side to simulate the transition from the traction condition to the regenerative braking condition. After a short adjustment of the voltage and current on the grid side, the operation is changed from the same phase to the reverse phase. The four-quadrant pulse rectifier can realize the operation of unit power factor, indicating that the dynamic performance of the control system is good. Figure 12(c) shows the power factor curve of the AC side of the rectifier. It can be seen from the figure that the power factor is close to 1 in both traction and braking conditions, which fully meets the operation requirements of the four-quadrant pulse rectifier.

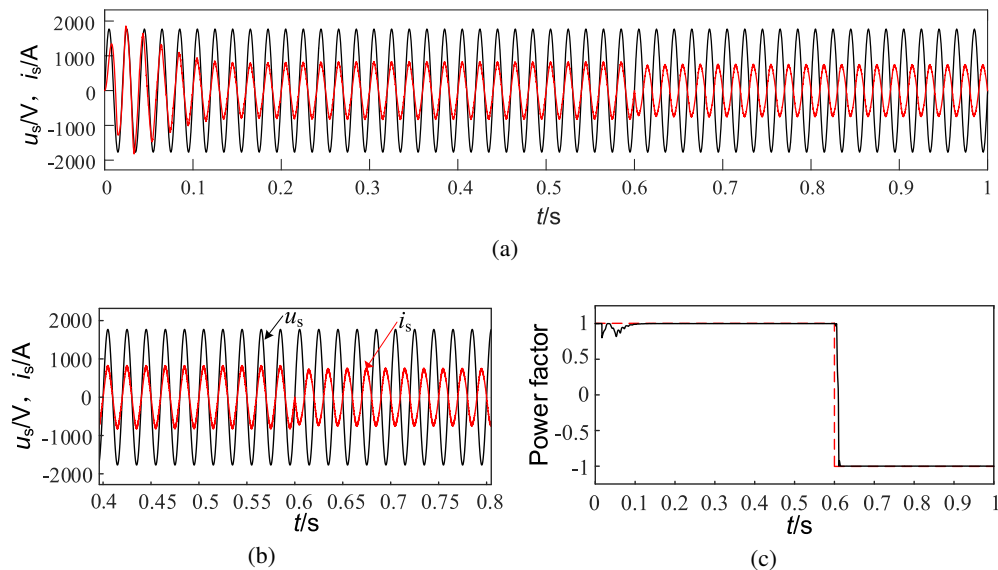


Fig. 12. The voltage and current waveform of transforming from traction condition to braking condition at $t = 0.6$ s (a); amplification of voltage and current waveform near $t = 0.6$ s (b); comparison of ideal and actual power factor curves (c)

5.2. Simulation verification of low-order harmonic current suppression

1. Simulation results with LC resonant circuit

Figure 13 shows the grid-side current waveform and FFT analysis results of the four-quadrant pulse rectifier when the LC resonant circuit is retained at the DC side. Figure 13(b) shows that after the LC resonance circuit is added to the DC side of the rectifier, the harmonic distortion rate of the current at the grid side is 2.57%. The 3rd harmonic of the current at the grid side accounts for 0.81%, the 5th harmonic is 0.06%, and the 7th harmonic is 0.03%.

When the LC resonant circuit is retained, the output voltage waveform of the DC side of the four-quadrant pulse rectifier is shown in Fig. 14. As can be seen from the figure, after 0.4 s, the DC voltage output by the rectifier can well track its given value 3 600 V, and its fluctuation range is about 3 578–3 624V.

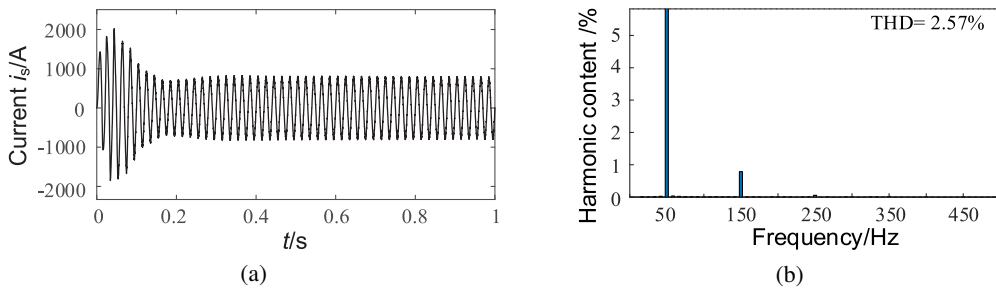


Fig. 13. Current waveform and FFT analysis results of grid side with LC resonant circuit at DC side: current waveform at the grid side (a); FFT analysis results of grid side current (b)

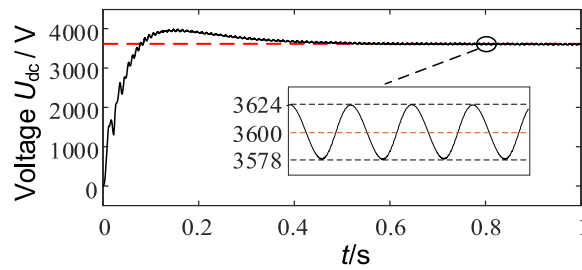


Fig. 14. DC side voltage waveform with LC resonant circuit

2. Simulation results without LC resonant circuit

Figure 15 shows the grid-side current waveform and FFT analysis results of the four-quadrant pulse rectifier after the LC resonant circuit is cancelled at the DC side. Figure 15(b) shows that after the LC resonant circuit is ceased at the DC side of the rectifier, the harmonic distortion of the current at the grid side is large, with a distortion rate of 6.12%. The 3rd harmonic of the current at the grid side is as high as 5.43%, the 5th harmonic is 0.43%, and the 7th harmonic is 0.04%.

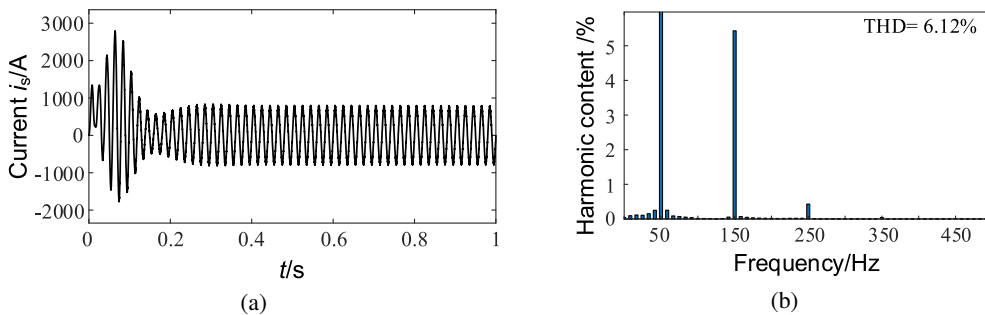


Fig. 15. Current waveform and FFT analysis results of grid side without LC resonant circuit at DC side: current waveform at the grid side (a); FFT analysis results of grid side current (b)

The output voltage waveform of the four-quadrant pulse rectifier on the DC side after disconnecting the LC resonance circuit is shown in Fig. 16. As can be seen from the figure, the DC-side voltage fluctuates greatly at a given value of 3 600 V, in the range of 3 519 V–3 684 V.

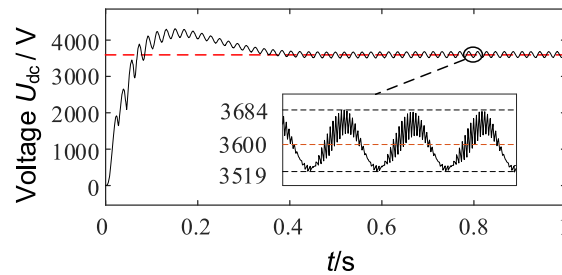


Fig. 16. DC side voltage waveform without LC resonant circuit

3. Simulation results of notch filter + PR controller

The notch filter has the function of filtering out harmonic components of a specific frequency, and its transfer function is shown in Eq. (31):

$$G(s) = A_0 \frac{s^2 + \omega_n^2}{s^2 + \frac{\omega_n s}{Q} + \omega_n^2}, \quad (31)$$

where A_0 represents the gain of the notch filter, and $A_0 = 1$ is taken in this paper. Q is the quality factor, ω_n is the characteristic angular frequency.

Therefore, notch filters with 200π (rad/s), 400π (rad/s) and 600π (rad/s) characteristic angular frequencies in series were used to eliminate the voltage ripple components of 2, 4 and 6 times grid frequency in the output DC voltage and indirectly suppress the low-order current harmonics.

Figure 17 shows the grid-side current waveform and FFT analysis results obtained by adding a notch filter to the voltage outer loop to eliminate the beat frequency voltage in the DC voltage after the LC resonant circuit was disconnected on the DC side of the four-quadrant pulse rectifier, and PR controller was adopted in the current inner loop. It can be seen from Fig. 17(b) that the

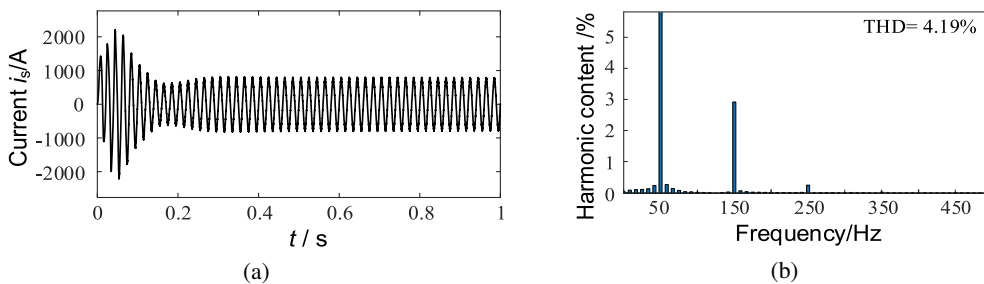


Fig. 17. Current waveform and FFT analysis results of grid side after using notch filter + PR controller: current waveform at the grid side (a); FFT analysis results of grid side current (b)

current harmonic distortion rate under this control method is 4.19%, in which the 3rd harmonic of the current at the grid side is 3.03%, the 5th harmonic is 0.27%, and the 7th harmonic is 0.04%.

Figure 18 shows the DC voltage waveform of the rectifier after the notch filter +PR controller is adopted. As can be seen from the figure, the DC side voltage fluctuates around a given value of 3 600V after about 0.3 s, and its fluctuation range is 3570–3631 V.

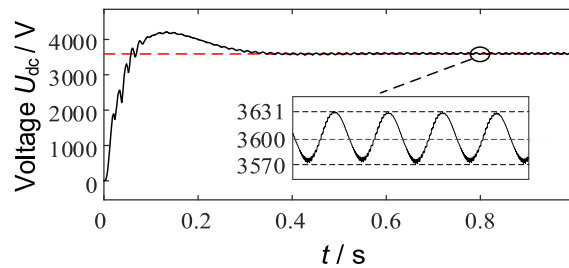


Fig. 18. DC side voltage waveform after using notch filter + PR controller

4. Simulation results of Butterworth filter and quasi-PR controller

Figure 19 respectively shows the current waveform on the grid side and the FFT analysis results when the Butterworth filter designed in this paper and the quasi-PR controller with 3rd, 5th and 7th harmonic compensation are used in the voltage outer loop and the current inner loop respectively after the LC resonant circuit is cancelled on the DC side of the rectifier. It can be seen from Fig. 19(b) that by using the optimization control method proposed in this paper, the harmonic distortion rate of grid-side current is reduced to 2.48%, in which the 3rd harmonic accounts for 0.22%, the 5th harmonic for 0.05%, and the 7th harmonic for 0.01%.

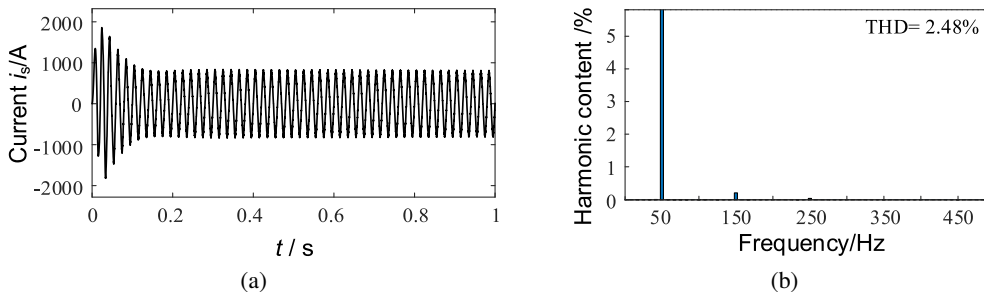


Fig. 19. Current waveform and FFT analysis results of using Butterworth filter and quasi-PR controller: current waveform at the grid side (a); FFT analysis results of grid side current (b)

The DC side voltage waveform of the rectifier after using the Butterworth filter and quasi-PR controller is shown in Fig. 20. As can be seen from the figure, after 0.2 s, the DC side voltage can well track the given value and stabilize at about 3 600 V, with the minimum fluctuation range of 3582–3621 V. Compared with Fig. 18, the time of voltage reaching steady state is shortened by about 1s, indicating that the dynamic performance of the system is significantly improved under the optimized control method.

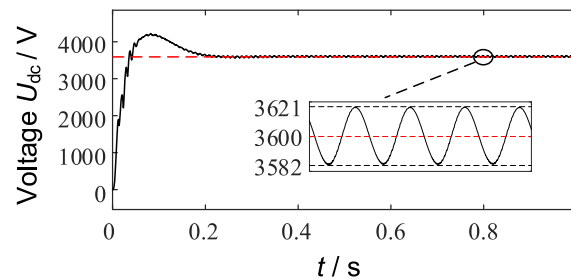


Fig. 20. DC voltage waveform of Butterworth filter and quasi-PR controller

According to the simulation results, the corresponding low-order current harmonic contents of the above four cases are summarized as shown in Table 3.

Table 3. Comparison of harmonic content of low-order current under different methods

The control method	3rd (%)	5th (%)	7th (%)	Total harmonic distortion rate (%)
Cancel the LC circuit	5.43	0.43	0.04	6.12
Notch filter + PR controller	3.03	0.27	0.04	4.19
Retain the LC circuit	0.81	0.06	0.03	2.57
Butterworth filter + quasi-PR controller	0.22	0.05	0.01	2.48

6. Conclusions

In this paper, aiming at the problem that a large number of low-order current harmonics occur on the grid side after the LC resonance circuit is disconnected on the DC side of the four-quadrant pulse rectifier in the traction drive system of some EMUs, the optimal control strategy of the four-quadrant pulse rectifier is proposed to effectively suppress the low-order current harmonics, and the simulation verification is carried out on the Matlab/Simulink platform. According to the simulation results, the following conclusions are drawn:

1. The optimized control strategy of the Butterworth filter and quasi-PR controller with harmonic compensation can effectively improve the dynamic performance of the control system, so that the four-quadrant pulse rectifier can quickly switch between traction and regenerative braking conditions, and realize the operation of unit power factor.
2. Since the notch filter can only filter the beat frequency voltage component at a specific frequency, and the Butterworth filter designed in this paper can filter the beat frequency voltage at 80 Hz and above, this means that the Butterworth filter has a better beat frequency voltage suppression effect on the DC side voltage than notch filter. It can reduce the influence

of DC side beat frequency voltage on the low-order harmonic current and indirectly suppress the low-order harmonic current of the grid side.

3. As can be seen from the data in Table 3, compared with the method of the notch filter + PR controller, the optimal control strategy based on the Butterworth filter and quasi-PR controller with harmonic compensation is more effective in suppressing the low-order current harmonics at the grid side, and the effect is similar to that when the LC resonant circuit is retained at the DC side of the rectifier. Therefore, the proposed optimal control strategy can completely replace the LC resonance circuit to meet the lightweight requirements of high-speed trains.

Acknowledgements

This research was supported by the National Natural Science Foundation of China (No. 52067013), the Natural Science Foundation of Gansu Province (No.20JR5RA395) as well as the Tianyou innovation team of Lanzhou Jiaotong University (TY202010).

References

- [1] Zhang Maosong, Chi Bangxiu, Li Jiawang et al., *Study on quasi-PR current coordinated control for active power filter*, Power System Technology (in Chinese), vol. 43, no. 5, pp. 1614–1623 (2019), DOI: [10.13335/j.1000-3673.pst.2018.0762](https://doi.org/10.13335/j.1000-3673.pst.2018.0762).
- [2] Laggoun Zakaria El Zair, Benalla Hocine, Nebti Khalil, *Dual Virtual Flux-based Direct Power Control for rectifier under harmonically distorted voltage condition*, Archives of Electrical Engineering, vol. 69, no. 4 (2020), DOI: [10.24425/AEE.2020.134641](https://doi.org/10.24425/AEE.2020.134641).
- [3] Song Zhiwei, Huang Lu, Xiong Chenglin et al., *Improved model predictive current control strategy for single-phase pulse rectifier*, Power System Technology (in Chinese), vol. 44, no. 5, pp. 1845–1851 (2020), DOI: [10.13335/j.1000-3673.pst.2018.3016](https://doi.org/10.13335/j.1000-3673.pst.2018.3016).
- [4] Milasi Rasoul M., Lynch Alan F., Yunwei Li, *Adaptive control of an active power filter for harmonic suppression and power factor correction*, International Journal of Dynamics and Control, vol. 10, pp. 473–482 (2022), DOI: [10.1007/S40435-021-00825-0](https://doi.org/10.1007/S40435-021-00825-0).
- [5] Hu HeJun, Wang JunJia, Huang YiYun et al., *Analysis and Suppression of Harmonic Characteristic for Multi-pulse Rectifier Based on Phase-shifting Transformer*, Journal of Physics: Conference Series, vol. 2237, no. 1 (2022), DOI: [10.1088/1742-6596/2237/1/012003](https://doi.org/10.1088/1742-6596/2237/1/012003).
- [6] Tamaskani Rohollah, Khodsuz Masume, Yazdani Asrami Mohammad, *Optimal Design of C-Type Filter in Harmonics Polluted Distribution Systems*, Energies, vol. 15, no. 4, pp. 1587–1587 (2022), DOI: [10.3390/EN15041587](https://doi.org/10.3390/EN15041587).
- [7] Hang Yin, Zhiyong Dai, Xianzhang Lei, Tian Lan, *Grid current low-order harmonics suppression of the three-phase grid converter with an LCL filter under the distorted grid voltage*, The Journal of Engineering, vol. 2019, no. 7, pp. 4675–4680 (2019), DOI: [10.1049/joe.2018.8037](https://doi.org/10.1049/joe.2018.8037).
- [8] Wang Shunliang, *Harmonic suppression and modulation method research for multilevel grid-side converter in electric railway traction*, Master Thesis, Southwest Jiaotong University, Chendu (2016).
- [9] Zhang Wen Ming, Li Yong Xin, Ge Xing Lai et al., *Optimized Design of Double-Loops Controller for Single-Phase Pulse Rectifier without LC Resonant Filter Circuit*, Advanced Materials Research, vol. 1061–1062, pp. 1031–1038 (2014), DOI: [10.4028/WWW.SCIENTIFIC.NET/AMR.1061-1062.1031](https://doi.org/10.4028/WWW.SCIENTIFIC.NET/AMR.1061-1062.1031).
- [10] Gitanjali Pandove, Ashutosh Trivedi, Mukhtiar Singh, *Repetitive control-based single-phase bidirectional rectifier with enhanced performance*, IET Power Electronics, vol. 9, no. 5, pp. 1029–1036 (2016), DOI: [10.1049/iet-pel.2015.0282](https://doi.org/10.1049/iet-pel.2015.0282).

- [11] Ali Muhammad Saqib, Wang Lei, Chen Guozhu, *Design and control aspect of segmented proportional integral repetitive controller parameter optimization of the three phase boost power factor correction rectifier*, International Journal of Circuit Theory and Applications, vol. 49, no. 3, pp. 554–575 (2020), DOI: [10.1002/CTA.2896](https://doi.org/10.1002/CTA.2896).
- [12] Phonsit Santiprapan, Apidet Booranawong, Kongpol Areerak *et al.*, *Adaptive repetitive controller for an active power filter in three-phase four-wire systems*, IET Power Electronics, vol. 13, no. 13 (2020), DOI: [10.1049/iet-pel.2019.1401](https://doi.org/10.1049/iet-pel.2019.1401).
- [13] Xiao Xiong, Wu Yujuan, Sun Guangda *et al.*, *Voltage-sensorless model predictive power control of PWM rectifier based on adaptive neural network observation*, Proceedings of the CSEE, vol. 41, no. 3, pp. 1135–1146 (2021), DOI: [10.13334/j.0258-8013.pcsee.200926](https://doi.org/10.13334/j.0258-8013.pcsee.200926).
- [14] Kang Longyun *et al.*, *Model Predictive Current Control with Fixed Switching Frequency and Dead-Time Compensation for Single-Phase PWM Rectifier*, Electronics, vol. 10, no. 4 (2021), DOI: [10.3390/ELECTRONICS10040426](https://doi.org/10.3390/ELECTRONICS10040426).
- [15] Tianbao Song *et al.*, *Suppression Method of Current Harmonics for Three-phase PWM Rectifier in EV Charging System*, IEEE Transactions on Vehicular Technology, vol. 69, no. 9 (2020), DOI: [10.1109/tvt.2020.3005173](https://doi.org/10.1109/tvt.2020.3005173).
- [16] Meng Wang *et al.*, *A modified sliding-mode controller based mode predictive control strategy for three-phase rectifier*, International Journal of Circuit Theory and Applications, vol. 48, no. 10, pp. 1564–1582 (2020), DOI: [10.1002/cta.2858](https://doi.org/10.1002/cta.2858).
- [17] Song Wensheng, Jiang Wei, Liu Bi *et al.*, *Single-phase cascaded H-bridge rectifiers simplified model predictive current control*, Proceedings of the CSEE, vol. 39, no. 4, pp. 1127–1138 (2019), DOI: [10.13334/j.0258-8013.pcsee.180205](https://doi.org/10.13334/j.0258-8013.pcsee.180205).
- [18] Ma Junpeng *et al.*, *Model Predictive Direct Power Control for Single Phase Three-Level Rectifier at Low Switching Frequency*, IEEE Transactions on Power Electronics, vol. 33, no. 2, pp. 1050–1062 (2018), DOI: [10.1109/tpel.2017.2681938](https://doi.org/10.1109/tpel.2017.2681938).
- [19] Wang Na, Mu Yuanpeng, *Harmonic current elimination for rectifiers based on n times notch filter and PR controller*, Electric Drive for Locomotives, vol. 2, no. 16, pp. 61–66 (2015), DOI: [10.13890/j.issn.1000-128x.2015.02.016](https://doi.org/10.13890/j.issn.1000-128x.2015.02.016).
- [20] Xiaohong Wang, Zhifeng Pan, Thi Thu Giang Hoang *et al.*, *New Repetitive Current Controller for PWM Rectifier*, IFAC PapersOnLine, vol. 51, no. 4, pp. 154–159 (2018), DOI: [10.1016/j.ifacol.2018.06.118](https://doi.org/10.1016/j.ifacol.2018.06.118).
- [21] Chen K.C. *et al.*, *Single phase inverter system using proportional resonant current control*, International Journal of Power Electronics and Drive Systems, vol. 8, no. 4, pp. 1913–1918 (2017), DOI: [10.11591/ijpeds.v8i4.pp1913-1918](https://doi.org/10.11591/ijpeds.v8i4.pp1913-1918).
- [22] Zhang Ying, Wang Huimin, Ge Xinglai *et al.*, *DC-link stabilization method for metro traction converter-motor system based on feedforward voltage compensation*, Proceedings of the CSEE, vol. 38, no. 9, pp. 2728–2735+2842 (2018), DOI: [10.13334/j.0258-8013.pcsee.171145](https://doi.org/10.13334/j.0258-8013.pcsee.171145).
- [23] Bi Kai *et al.*, *Virtual Flux Voltage-Oriented Vector Control Method of Wide Frequency Active Rectifiers Based on Dual Low-Pass Filter*, World Electric Vehicle Journal, vol. 13, no. 2 (2022), DOI: [10.3390/WEVJ13020035](https://doi.org/10.3390/WEVJ13020035).
- [24] Liu Jianqiang, Liu Chuanduo, Wang Yiyou *et al.*, *Fault diagnosis method for IGBT and DC-link capacitor of single-phase PWM rectifier*, Transactions of China Electrotechnical Society, vol. 34, no. S1, pp. 244–257 (2019), DOI: [10.19595/j.cnki.1000-6753.tces.L80029](https://doi.org/10.19595/j.cnki.1000-6753.tces.L80029).
- [25] Majer K., *The analysis of vibration of smoothing reactors working in single-phase rectifier systems*, Przegląd Elektrotechniczny (in Polish), vol. 95, no. 8, pp. 53–56 (2019), DOI: [10.15199/48.2019.08.14](https://doi.org/10.15199/48.2019.08.14).